LONG-TERM ANALYTICAL ORBIT DECAY AND REENTRY PREDICTION

H.H. Klinkrad

Earth Observation Programme Department
ESA / ESTEC, Noordwijk, The Netherlands

ABSTRACT

The present paper outlines the main features of a new analytical approach to the prediction of close-earth satellite orbits of moderate eccentricities. Based on the method of general averaging and on the principle of separation of perturbations, known results for the averaged time rates of change of the mean orbital elements due to J_2, J_3, and J_4 are superimposed with new results of the averaged airdrag perturbation equations to obtain the total rates, which are then used to propagate the mean Kepler state in step-sizes of 1 to 15 orbits.

The improved airdrag model incorporates in an analytically integrable representation a rotating atmosphere, a variable aerodynamically effective satellite cross-section, and a comprehensive, state-of-the-art MSIS'77 (Ref.3) derived air density model as function of all major atmospheric parameters.

Keywords: Analytical Orbit Prediction, Reentry Prediction, Mean Elements, Air Density Model, Airdrag Model, Method of Variation of Orbital Elements.

1. INTRODUCTION

When dealing with the problem of close-earth satellite orbit prediction, one can distinguish two principle approaches which are the analytical and the numerical type orbit generators respectively. Both of these approaches have certain advantages as well as disadvantages, which shall be briefly reviewed :

While on one hand numerical orbit prediction methods provide highly accurate results and allow for perturbation models of arbitrary complexity, this accuracy and model fidelity is achieved at the expense of computer time consumption, because the state propagation in this case follows the high frequency short periodic variation functions of the six osculating Kepler orbital elements (see Fig.3-1b). The relatively small permissible step-size of only 1/80 to 1/50 of the orbital period, corresponding to typically 2 minute time steps, and the likewise high number of perturbation function evaluations (after each step) are consequently leading to considerable computing (CPU) times.

In contrast with numerical integrators, analytical orbit prediction methods initially transform a given osculating state to a mean state which is then subject only to long-periodic and secular effects in case of singly averaged elements (averaged with respect to M), or subject only to secular perturbation effects in case of doubly averaged elements (averaged with respect to mean anomaly M and argument of perigee ω, see Fig.3-1b). Singly averaged elements, which will be of concern in this paper, are then propagated in time along the smoothed, long-periodic individual variation functions. The permissible step-size in this case can be of the order of 1 orbit to 1 day, depending on the instantaneous perturbation level. This considerable increase in time step versus a numerical method is reflected in a corresponding decrease of computing time. Some of this gain, however, is lost for the transformations from osculating to mean elements, for the back-transformations, and for the formulation and analytical integration of the averaged equations of motion. Moreover, the necessity for an integrable set of perturbation equations is in most analytical theories accounted for by over-simplified and hence inaccurate models of the perturbation environment (this is especially true for airdrag).

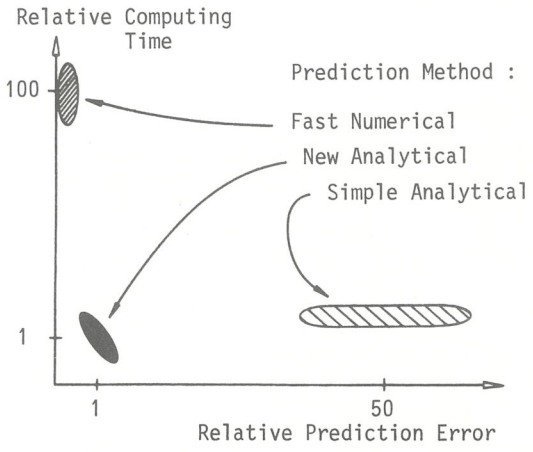

Fig.1-1 : Relative Computing Time and Prediction Error of a Fast Numerical Method, a Simple Analytical, and a Projected, New Analytical Theory for Orbit Prediction.

The achievable performances of typical fast numerical and conventional analytical orbit prediction methods are depicted as function of relative CPU time consumption and relative prediction error in Fig.1-1. It is the intention of this paper, to deploy the theoretical baseline of a new analytical prediction approach for close-earth satellite orbits (between about 120 and 1000 km of altitude), which to a large extend incorporates the advantages of both numerical and analytical methods, providing results of a precision close to that of numerical integrations within computing times close to those of simple analytical theories.

The performance of the new method will first be verified with respect to reference results of a numerical integration, and with respect to results of a simple analytical theory for a well-defined orbit perturbation environment. The validity of the solution approach will then also be demonstrated for a weakly defined perturbation environment in context with an orbit decay and reentry prognosis for the satellite fragments COSMOS 1402A and 1402C which reentered the atmosphere on Jan.23 and Feb.7, 1983, respectively.

2. MODELLING OF THE RELEVANT ORBIT PERTURBATIONS

The effective perturbing acceleration acting on a close-earth satellite orbit can be sufficiently modelled by superimposition of the effects of the first and second order earth oblateness potential, and of the second order non-conservative (i.e.: energy dissipating) airdrag force. (Def.: a perturbation is of order "j", if its relative magnitude is 10^{-3j} of the local central attraction term g.)

2.1 Earth Oblateness Perturbation Model

The perturbing acceleration due to inhomogenities of the geopotential can be modelled by means of an expansion in spherical harmonic functions with earth-specific harmonic coefficients. In order to attain a second order accuracy for this approximation, it proves sufficient to consider the first three zonal harmonics J_2, J_3, and J_4 only, which represent the rotationally symmetric deformations (also denoted as earth oblateness potential, see Fig.2-1). According to the previously adopted definition, J_2 gives rise to first order while J_3 and J_4 give rise to second order gravity perturbations. The corresponding perturbation magnitude is given by

$$\underline{p}_G = -\,\mathrm{grad}\left[\ \mu/r \sum_n J_n (a_e/r)^n P_n(\sin\phi)\ \right] \qquad (2.1)$$

$$|\underline{p}_G| \approx 10^{-3}\ g \qquad (2.2)$$

where
- r - geocentric satellite distance
- a_e - normalising earth equatorial radius
- J_n - n-th zonal harmonic (see Fig.2-1)
- ϕ - geocentric latitude
- P_n - Legendre function of degree n and argument $\sin\phi$
- μ - earth gravitational constant (central attraction term = 3.986e+14 m^3/s^2)

with
- J_2 = 1082.6268e-6
- J_3 = - 2.5356e-6
- J_4 = - 1.6234e-6
- J_5 = - 0.2276e-6
- ⋮

where the harmonics J_n are adopted from GEM-10 (Goddard Earth Model 10).

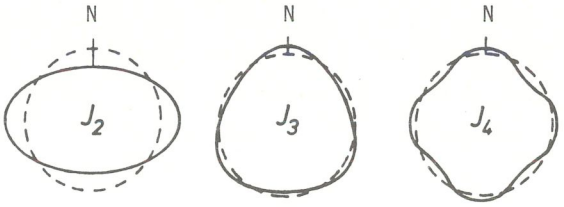

Fig.2-1: First (J_2) and second order (J_3 and J_4) contributions to the perturbing earth oblateness potential.

2.2 Airdrag Perturbation

The airdrag deceleration is acting opposite to the relative velocity vector of a satellite passing through the rotating earth atmosphere. The direction and magnitude of the airdrag perturbation are described by

$$\underline{p}_D = -\frac{1}{2} c_D \frac{A}{m} \rho\, V_r \underline{V}_r \qquad (2.3)$$

where
- c_D - satellite drag coefficient
- A - aerodynamically effective cross-section
- m - satellite mass
- $\underline{V}_r = \dot{\underline{r}} - \underline{\omega}_e \times \underline{r}$ - relative velocity vector of magnitude V_r (magnitude of $\omega_e \cong 2\pi$/day)
- ρ - local air density

Generally, for satellite altitudes above 200km, airdrag can be regarded as a second order perturbation. Only shortly before final reentries, at altitudes below 120km, it may attain the same magnitude as the first order J_2 earth oblateness acceleration (see Fig.2-2), in which case analytical orbit theories fail, and predictions should be continued by means of numerical methods which are able to follow the transition from orbital to sub-orbital and finally to atmospheric flight conditions.

The present paper, however, will focus on a regime of well-defined orbit mechanics at satellite altitudes well above 120 - 130km. In order to prepare the grounds for an analytical integration of the relevant perturbation equations (with due regard to airdrag), the major drag force parameters ρ, A, and c_D shall now be analysed in more detail.

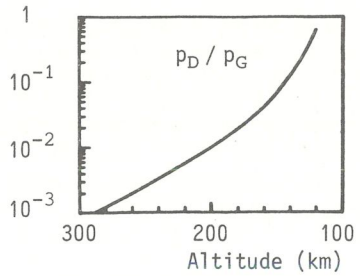

Fig.2-2: Relative magnitude of the airdrag deceleration with respect to the first order earth oblateness perturbation for a typical satellite at altitudes below 300km.

2.2.1 Air Density

The main driver which determines air densities beyond 120km of altitude is the heterospheric temperature profile T(h) as shown in Fig.2-3. The shape

of this profile can be described by an exponential function, starting with a steep increase of T at 120km, and reaching an asymptotic limit, the exospheric temperature T_∞, above the thermopause. The mathematical expression for the temperature altitude profile model is

$$T(h) = T_\infty - (T_\infty - T_{120}) \cdot \exp[-s \cdot (h-120)] \quad (2.4)$$

where T_∞ - exospheric temperature
T_{120} - initial, steady temperature at 120km
s - temperature gradient parameter in 1/km
h - geodetic altitude in km

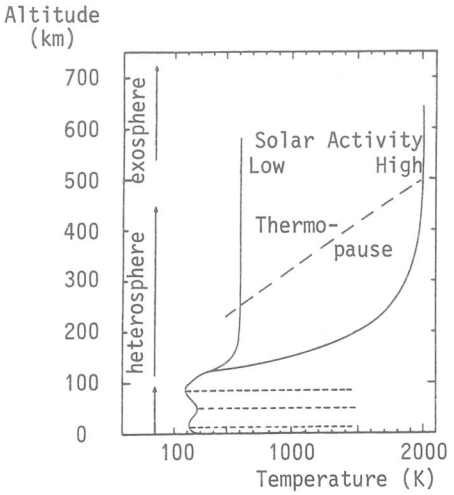

Fig.2-3: Temperature altitude profile of the atmosphere for high and low solar activity levels (high and low exospheric temperatures T_∞).

The 2-dimensional model (2.4) becomes a 3-dimensional, time dependent function after introducing observed variations of its coefficients as function of the following atmospheric parameters:

- local geodetic altitude
- local solar time (pronounced periods: 1d, 1/2d)
- local geodetic latitude
- season (pronounced periods: 1Y, 1/2Y)
- actual solar activity $F_{10.7}$ (10.7cm solar radio flux)
- mean solar activity $\bar{F}_{10.7}$ (average of $F_{10.7}$ over 3 or 6 solar revolutions = 81d or 162d ; with pronounced period of 11Y = 1 solar cycle)
- geomagnetic activity A_p (Bartels index)

As indicated in Fig.2-3, the shape as well as the asymptotic limit of the temperature profile are predominantly depending on the solar activity level. For high and low solar fluxes respectively the exospheric temperature T_∞ may range from 600K to 1900K.

Assuming the existence of a diffusive equilibrium within the heterosphere, and assuming furthermore a temperature profile T(h) according to (2.4), the individual particle concentrations n_j of the major atmospheric constituents N_2, O, O_2, He, Ar and H under the influence of the gravitational field and the temperature gradient settle in exponential altitude profiles which can be described by the following diffusion equations

$$n_j(h) = n_{j,120} \; [T_{120}/T(h)]^{1+\alpha_j} \; \exp[-\int_{120}^{h} \frac{M_j g}{R\,T} dh] \quad (2.4)$$

where j = 1,2,3,4,5,6 for N_2, O, O_2, He, Ar, H
$n_{j,120}$ - initial particle concentration at 120km altitude for constituent j
α_j - thermal diffusion coefficient (= -0.4 for He,H and 0.0 otherwise)
M_j = 18,16,32,4,40,1 for N_2, O, O_2, He, Ar, H
- mass number of constituent j
g - gravity acceleration g(h)
R - universal gas constant

Fig.2-4a,b show the logarithmic gradients of these individual concentration profiles as function of mass number and exospheric temperature level for geodetic and geopotential altitudes up to 2000km. These logarithmic gradients which are directly proportional to M_j and inversely proportional to T(h) are denoted as concentration scale heights.

$$\frac{d}{dh}[\ln(n_j)] = -\frac{M_j g(h)}{R\,T(h)} \quad (2.6)$$

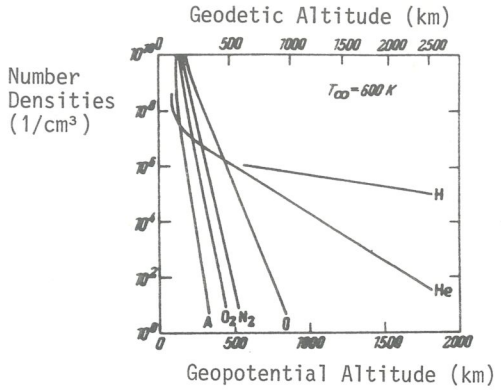

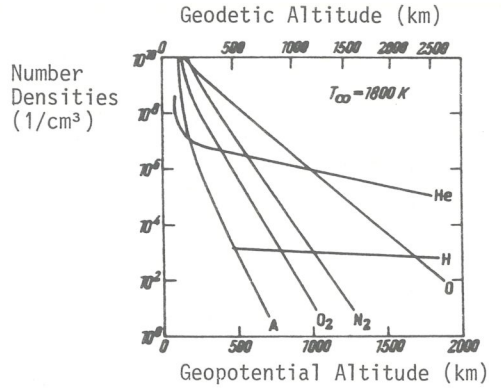

Fig.2-4a,b: Concentration altitude profiles of the six major constituents of the heterosphere for low (Fig.2-4a, top) and high exospheric temperature (Fig.2-4b, bottom) respectively.

The sought air density distribution finally results from superimposition of the individual concentration profiles, weighted by their respective mass numbers, and divided by Avogadro's number.

$$\rho(h) = \frac{1}{A} \sum_j n_j \cdot M_j \quad (2.7)$$

As was true for the temperature profile (2.4), also the concentration profiles (2.5) are described by coefficients which exhibit a 3-dimensional, time dependent variation characteristic, and which consequently lead to a likewise 3-dimensional, time dependent air density distribution function (2.7).

The complicated interaction of the individual number densities results in a very complex air density variation which as function of short-periodic (diurnal), long-periodic (seasonal), and very long-periodic (solar cycle) effects is illustrated in Fig. 2-5a through 2-5d for a constant altitude of 400km within a local solar time and latitude grid. Evidently, in spite of similar locations of the diurnal maxima close to 15h local solar time, each of the density distribution functions shows very specific characteristics in terms of shape, mean value, and variation amplitude. - Consequently, in order to avoid significant modelling errors, the projected analytical orbit prediction theory shall take into account a state-of-the-art dynamic air density model (e.g.: MSIS77, Ref.3) as function of all of the above mentioned atmospheric parameters.

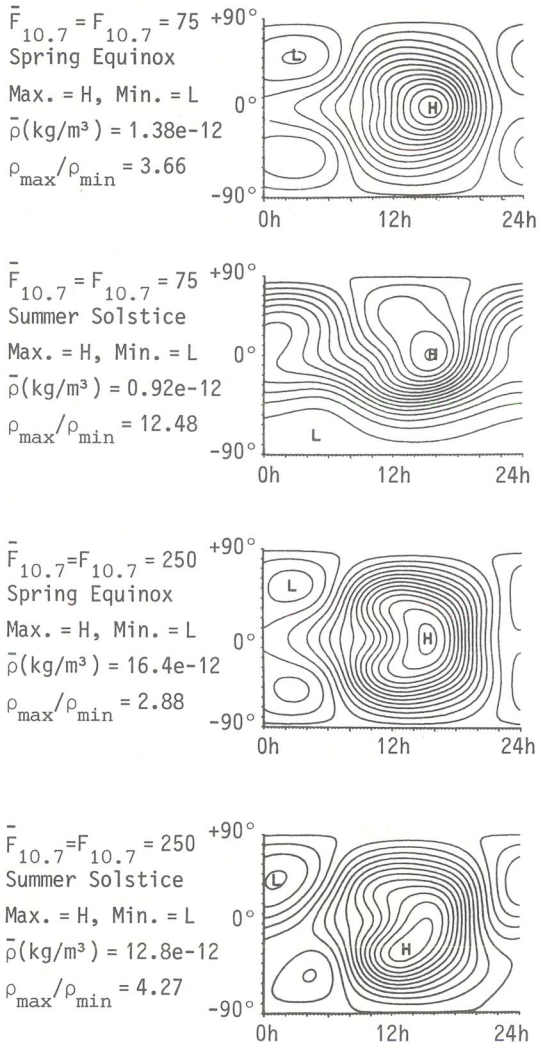

Fig.2-5a,b,c,d: Short-periodic (diurnal), long-periodic (seasonal), and very long-periodic (solar cycle) air density variations for a constant altitude of 400km as function of local solar time and latitude (according to MSIS77, Ref.3).

2.2.2 Aerodynamically Effective Satellite Cross-Section

Most satellites are attitude stabilised in one way or another. If the stabilisation is done with respect to an inertial frame (e.g. star telescopes) or with respect to a quasi-inertial frame (e.g. solar array pointing), then the aerodynamically effective cross-section of a spacecraft travelling through the earth atmosphere experiences variations which are predominantly periodic with the mean orbital motion. The aerodynamical cross-section of the future European Retrievable Carrier EURECA, for instance, can be idealised by a non-varying (i.e.: spherical) central body cross-section of about 4m², with attached, truely sun-pointing solar arrays of approximately 80m² (1982 figures). Neglecting aerodynamical shielding, the cross-section variation function would be (see Fig.2-6a)

$$A_x = A_o + A_p \, | \cos \Phi | \qquad (2.8)$$

where A_o - constant cross-section of central body
A_p - total projected surface of solar arrays
Φ - incidence angle of airflow on arrays

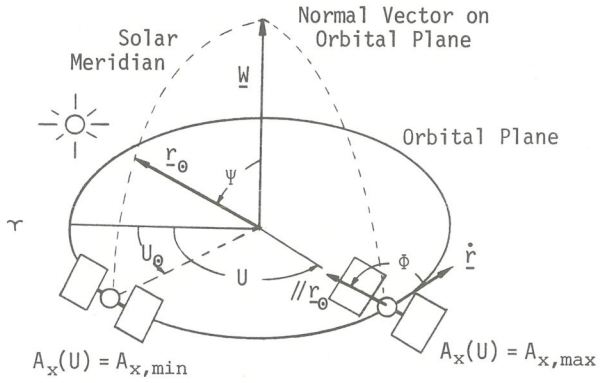

Fig.2-6a: Effective aerodynamic cross-section of a spherical satellite with truely sun-pointing solar arrays as function of short (→ U) and long periodic (→ Ψ) effects.

The periodic part of A_x according to (2.8) can be recognised as the result of a short-periodic variation, with a period of 1/2 revolution, of which the amplitude varies long-periodically with the annual solar motion and the precession of the orbital plane. This periodicity is illustrated in Fig.2-6a and 2-6b, and can be expressed as

$$A_x = A_o + A_p \sin \Psi \, | \sin(U - U_\odot) | \qquad (2.9)$$

2.2.3 Satellite Drag Coefficient

The satellite drag coefficient c_D in (2.3) can be regarded as a calibration factor, reflecting properties of the satellite surface and geometry, the ambient atmosphere, the velocity of the impinging particles, and the relative velocity of the spacecraft. During the lifetime of a close-earth satellite, c_D successively is (1) a function of the Knudsen number Kn in the regime of free and disturbed molecular flow, (2) a function of the Mach number Ma in the phase of hypersonic to subsonic speeds, and (3) in few cases a function of the

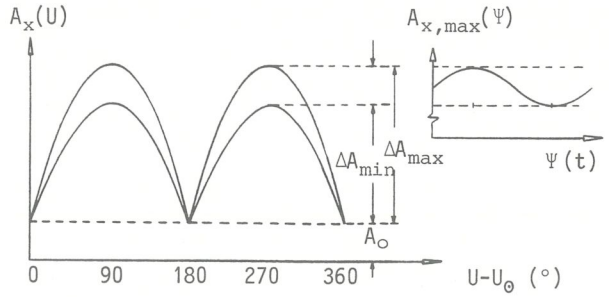

Fig.2-6b: Short-periodic cross-section variation with long-periodically changing amplitude for a spherical satellite with truely sun-pointing solar arrays.

Reynolds number Re shortly before impact.

When focussing on orbit decay predictions at altitudes well above 120km, for most satellites (except for large space structures) the conditions of free molecular flow are met, and analysis of corresponding orbits indicates that c_D can be sufficiently modelled by a constant value of 2.2 . This figure shall also be adopted in the forthcoming analysis.

Especially in context with lifetime predictions for satellites of unknown geometry and mass a lumped expression for the drag coefficient c_D and the area-per-mass ratio A/m proves to be useful, which is denoted as the ballistic parameter B of the spacecraft.

$$B = c_D \cdot A/m \qquad (2.10)$$

3. ANALYTICAL ORBIT PREDICTION APPROACH

3.1 The Method of Variation of Orbital Elements

One of the elementary results of kinematics implies that the instantaneous state of motion of a point mass within an inertial frame at a certain time t can be uniquely defined by a state vector $\underline{x}(t)$, consisting of the six components in total of the instantaneous position and velocity vector, or alternatively, in case of orbital motion, by a corresponding set of six Kepler elements (a,e,i,Ω,ω and M).

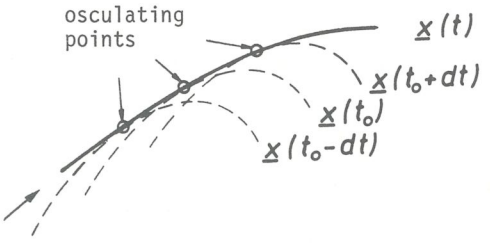

Fig.3-1a: Approximation of a true, perturbed orbit arc $\underline{x}(t)$ by infinitesimal segments of individual, unperturbed Kepler orbits with time varying orbital elements.

When considering a Kepler motion, with the earth idealised as a point mass, the satellite is moving on a plane ellipse of non-varying shape and constant orientation within an inertial frame. In the presence of a small perturbation force, however, the satellite orbit is no longer a pure, plane ellipse, but the envelope of an infinite sequence of individual unperturbed Kepler arcs, which in themselves describe the state of motion in the close vicinity of a tangent, osculating point by a distinct set of osculating elements $\underline{x}(t_o)$. The infinitesimal transition from one of these osculating arcs at time t_o to the next following at time t_o+dt can be described by a simple point-slope formula.

$$x_i(t_o+dt) = x_i(t_o) + \dot{x}_i(t_o)\, dt \qquad (3.1)$$

where $\underline{x} = (x_1,x_2,\ldots,x_6) = (a,e,i,\Omega,\omega,M)$

$i = 1,2,\ldots,6$

The required time rates of change $\dot{x}_i$ of the orbital elements can be determined by means of the Lagrange planetary equations in their Gaußian formulation as function of the instantaneous osculating elements $x_i(t_o)$ and the perturbing acceleration $\underline{p}(t_o)$, which for close-earth satellite orbits results from a superimposition of the geopotential and airdrag perturbations $\underline{p}_G$ and $\underline{p}_D$ respectively.

$$\dot{x}_i(t_o) = fct_i(\underline{x}, \underline{p}_G, \underline{p}_D) \qquad (3.2)$$

This concept of time variant individual Kepler arcs for the extrapolation of the osculating state is known as the Method of Variation of Orbital Elements.

3.2 Numerical Versus Analytical Orbit Prediction Methods

When monitoring the variation of some orbital element with respect to time, one can identify three basic perturbation contributions from the aspect of periodicity. They are denoted as secular (time proportional), long-periodic (with periods of typically months), and short-periodic (with periods of the order of hours). The osculating elements $x_i(t)$, which at any instant reflect the true state of motion, result from a superimposition of all of these individual perturbation frequencies (see Fig.3-1b).

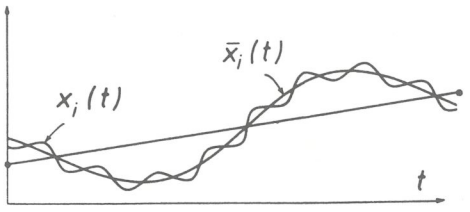

Fig.3-1b: Time development of osculating elements $\underline{x}_i(t)$ and singly averaged, mean elements $\bar{\underline{x}}_i(t)$ under the influence of secular, long-periodic, and short-periodic perturbation effects.

Numerical orbit prediction methods share the common principle to directly propagate the osculating state $x_i(t)$ by an extrapolation of the kind

$$x_i(t_o+\Delta t) = x_i(t_o) + \dot{x}_i(t_o)\, \Delta t \qquad (3.3)$$

where the perturbation equations $\dot{x}_i(t)$ are symbolically given by (3.2).

As a numerical integration according to (3.3) will have to follow the short-periodic ripples of the variation function $x_i(t)$ in Fig.3-1b, the employed step-size Δt for the propagation should not exceed about 1/50 of the orbital period in order to keep extrapolation errors to a minimum. Thus

$$\Delta t_{num} < 1/50\ T \approx 2\,min \qquad (3.4)$$

Broadly speeking, the simplicity of the state prediction approach (3.3) is conserved at the expense of computing effort, because for each propagation step an evaluation of the complex perturbation equations (3.2) has to be carried out.

In contrast with numerical methods, analytical orbit prediction theories strive for an increase in propagation step-size at the cost of a computation intensive preprocessing of the perturbation equations (3.2). In principle, analytical orbit theories proceed in four successive steps:

(1) Transformation from osculating to mean orbital elements by removal of short-periodic variations (→ singly averaged elements) and possibly long-periodic variations (→ doubly averaged elements).

(2) Determination of the time rates of change of the mean orbital elements as function of the instantaneous mean state and the perturbation environment.

(3) Propagation of the mean orbit state along the smooth, averaged variation functions with increased step-size (see Fig.3-1b).

(4) Retrieval of the true, osculating orbit state by a back-transformation.

3.3 Outline of a New Analytical Close-Earth Orbit Prediction Approach

The following analytical orbit prediction method is based on singly averaged Kepler elements, averaged over 2π of the mean anomaly M (see (3.10)). The set of six formulae for the implicit transformation from osculating elements x_i to mean elements $\bar{x}_i$, and the explicit back-transformation respectively can be expressed by the symbolic notations

$$\bar{x}_i(t_o) = x_i(t_o) - \Delta\bar{x}_i(\bar{\underline{x}}(t_o); J_2) \qquad (3.5)$$

$$x_i(t_o) = \bar{x}_i(t_o) + \Delta\bar{x}_i(\bar{\underline{x}}(t_o); J_2) \qquad (3.6)$$

The first order (J_2) transformation functions shall be adopted from Liu (Ref.4).

Once the mean orbit state is established, it can be propagated in time by a point-slope formula corresponding to (3.3) in the domain of mean elements.

$$\bar{x}_i(t_o+\Delta t) = \bar{x}_i(t_o) + \dot{\bar{x}}_i(t_o)\,\Delta t \qquad (3.7)$$

Due to the considerably smoother time variation of $\bar{x}_i(t)$ as compared with $x_i(t)$ (see Fig.3-1b), the propagation step-size may now be increased to as much as

$$\Delta t_{ana} \approx T \text{ to } 15\,T \;\triangleq\; 1.5h \text{ to } 1d \qquad (3.8)$$

where T is the orbital period. This big increase in step-size is the major advantage of analytic theories. It is achieved at the cost of additional effort in the determination of the averaged time rates of change of the mean Kepler elements which are defined as

$$\dot{\bar{x}}_i(t_o) = \frac{1}{2\pi}\int_0^{2\pi} \dot{x}_i(\bar{\underline{x}}(t_o); p_G, p_D)\, dM \qquad (3.9)$$

In order to solve this integral, it shall be assumed that the airdrag and geopotential perturbation effects can be averaged individually (→ separation of perturbations), and then be added to provide the effective time rates of change of the mean orbital elements. Assuming that airdrag is a second order perturbation, the error introduced by this approach is of third order only and may be neglected. One obtains

$$\dot{\bar{x}}_i(t_o) = \dot{\bar{x}}_{i,G}(t_o) + \dot{\bar{x}}_{i,D}(t_o) \qquad (3.10)$$

where

$$\dot{\bar{x}}_{i,G} = \frac{1}{2\pi}\int_0^{2\pi} \dot{x}_{i,G}(\bar{\underline{x}}(t_o); p_G)\, dM \qquad (3.10a)$$

$$\dot{\bar{x}}_{i,D} = \frac{1}{2\pi}\int_0^{2\pi} \dot{x}_{i,D}(\bar{\underline{x}}(t_o); p_D)\, dM \qquad (3.10b)$$

In this equation $\dot{\bar{x}}_{i,G}$ for each of the elements $\bar{x}_1$ to $\bar{x}_6$ is given up to second order geopotential perturbation level (J_2,J_2^2,J_3 and J_4) by Liu (Ref.4). The expression $\dot{\bar{x}}_{i,D}$ according to (3.10b), however, remains to be solved for a comprehensive airdrag model as outlined in 2.2. The following description of this solution summarises in a symbolic notation the results of a more rigorous analysis performed in Ref.1 and Ref.2.

One intends to average $\dot{x}_{i,D}$ in (3.10b) with respect to the mean anomaly M, however, in order to arrive at well-known integrals (→ Bessel functions, see (3.16/17)) the integration variable shall be the eccentric anomaly E. Hence, in a first step, $\dot{x}_{i,D}\,dM/dE$ (rather than $\dot{x}_{i,D}$) is expanded in a Poisson series of sine and cosine terms of the eccentric anomaly up to terms of order e^3 of the orbit eccentricity, including a simple airdrag model consisting of a uniformly rotating atmosphere, a spherically symmetric air density distribution with linearly varying scaleheight, a constant aerodynamic satellite cross-section, and a constant drag coefficient of 2.2. One gets

$$\dot{x}_{i,D}\,dM/dE = \exp(ae/H_\rho \cos E) \cdot \sum_r c_{ir}\cos(rE) + s_{ir}\sin(rE) + O(e^4) \qquad (3.11)$$

where ae is the linear eccentricity of the orbit, H_ρ is the density scale height, and c_{ir} and s_{ir} are reflecting the aforementioned assumptions.

In a second step, a correction factor K_x to (3.11) is derived which takes into account short and long-periodic aerodynamic cross-section variations. A good representation of the variation function shown in Fig.2-6b can already be obtained by the following Fourier expansion in E, where the coefficients represent information on satellite geometry and attitude, orbit plane orientation, and sun position.

$$K_x(E) = 1 + c_o + c_A\cos(2E) + s_A\sin(2E) \qquad (3.12)$$

In a third step, a correction factor K_ρ to (3.11) is determined which reflects diurnal air density variations along the orbit as function of the orbital elements, solar activity, and season. Using successive expansions in spherical harmonics, inclination functions, and eccentricity functions, the integration variable E can eventually be isolated, and the following explicit formulation is obtained.

$$K_\rho(E) = 1 + \sum_n \sum_m \sum_p \sum_q c_{nmpq}\cos(qE) + s_{nmpq}\sin(qE) \qquad (3.13)$$

Finally, in a fourth step, the seperately developed modules (3.11),(3.12) and (3.13) are concatenated using the trigonometric multiplication theorems. The dependence on the fast variable E can hereby be isolated and reduced to expressions of the sort

$$T_c(E) = \cos[(r\pm q)E]\cdot \exp(ae/H_\rho \cos E) \qquad (3.14)$$

$$T_s(E) = \sin[(r\pm q)E]\cdot \exp(ae/H_\rho \cos E) \qquad (3.15)$$

According to the definition of Bessel functions,

and due to the fact that $T_s(E)$ is an odd function, one finds

$$\frac{1}{2\pi}\int_0^{2\pi} T_c(E)\,dE = I_{r\pm q}(ae/H_\rho) \qquad (3.16)$$

$$\frac{1}{2\pi}\int_0^{2\pi} T_s(E)\,dE = 0 \qquad (3.17)$$

with $T_c(E)$ and $T_s(E)$ according to (3.14) and (3.15). Hence, upon integration of the concatenated modules of the airdrag model over 2π of the eccentric anomaly E (= averaging of the drag equations of motion with respect to M, see (3.11)), one arrives at the final notation

$$\dot{\bar{x}}_{i,D} = \sum_n \sum_m \sum_p \sum_q \sum_r \left[s_{nmpq} S_{ir} (I_{r-q} - I_{r+q}) + c_{nmpq} C_{ir} (I_{r-q} + I_{r+q}) \right] \qquad (3.18)$$

where

- s/c_{nmpq} - sine and cosine terms in E of the diurnal air density model (3.13)
- S/C_{ir} - sine and cosine terms in E of the series product (3.11)•(3.12)
- $I_{r\pm q}$ - modified Bessel functions of order $r\pm q$ and of argument ae/H_ρ
- n - degree of the diurnal air density spherical expansion model
- m - order of the diurnal air density spherical expansion model
- p - expansion order of inclination functions
- q - expansion order of eccentricity functions
- r - expansion order of the Poisson series in E of the simplified airdrag perturbation equations (3.11)

Finally, the effective time rate of change of the mean orbital elements according to (3.10) is determined by superimposition of the airdrag perturbation results due to (3.18) with compatible geopotential perturbation results obtained by Liu (Ref.4) taking into account J_2,J_2^2,J_3 and J_4 contributions.

This completes the derivation of the inputs which are necessary to propagate the mean orbit state by means of (3.7) and (3.10).

4. ASSESSMENT OF RESULTS

The outlined analytical close-earth orbit prediction theory has been implemented in a computer program denoted as APODES (Analytical Prediction of Orbit Decay for Earth Satellites). A critical assessment of this implemented theory shall in the following be performed under two different application aspects:

(1) For a well-defined orbit perturbation environment, assuming perfect knowledge of the gravitational and airdrag forces, an orbit decay analysis will be performed for EURECA (the European Retrievable Carrier). Results of the new theory will be compared with those of a numerical integration, and of an analytical approach with a simplified airdrag model.

(2) In a quasi-operational environment, for an orbit decay and reentry prognosis of COSMOS 1402-A and 1402-C, results of the new theory will be compared with aposteriori observed orbit data published in NASA Prediction Bulletins.

Appart from the prediction accuracy of the new theory, also the aspect of computing time will be addressed.

4.1 Orbit Prediction Accuracy in a Well-Defined Perturbation Environment

In order to demonstrate the capabilities of the outlined analytical orbit prediction method, a typical orbit of the future EURECA experimental platform will be analysed, using the following assumptions: orbit altitude of 400km, near-circular orbit of $\bar{e}$ = 0.001, inclination of 28.5° (launch from Cape Canaveral), idealised spherical satellite body of 4m² cross-section, truely sun-pointing solar arrays of projected area 80m² (1982 figures), a total mass of 2200kg, and a high solar activity level of $F_{10.7}$ = $\bar{F}_{10.7}$ = 200 (see Ref.2 for more details). Furthermore, in contrast with the intended mission operation, it shall be assumed that the solar arrays remain completely deployed throughout the flight. For these model assumptions Fig.4-1 shows the resulting variation of the drag deceleration magnitude over one orbit as function of local solar time for three different approaches:

(A) Numerical integration with exact representation of (2.3)

(B) New analytical theory (APODES) with (2.3) modelled as described by (3.11) - (3.13)

(C) Simple analytical theory using a mean satellite cross-section (averaged over one orbit), and no diurnal air density representation

From Fig.4-1 it can be seen that the new analytical model (B) provides a good approximation of the true drag force variation (A), while a simplified analytical approach (C) overestimates the mean drag force level.

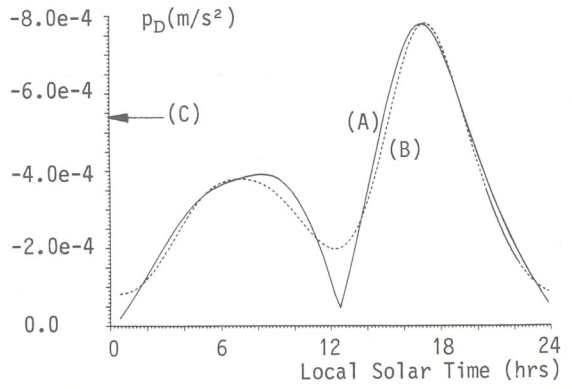

Fig.4-1: Short-periodic variation of the airdrag deceleration magnitude for EURECA as function of local solar time.
(A) numerical simulation (reference)
(B) new analytical model function
(C) simple analytical model

The accuracy by which the mean level of the drag force is modelled, is directly reflected by the accuracy for the prediction of the semimajor axis of the orbit which represents the orbit energy content and hence serves as a sensitive gauge for the energy dissipating drag deceleration. Fig.4-2 demonstrates that the predictions of the semimajor axis (and hence of the lifetime) of the orbit by numerical integration (A) and by the new theory (B) are in excellent agreement, while a simplified analytical algorithm (C) arrives at a reentry which is short by 7d with respect to the true, numerically computed lifetime of about 27d.

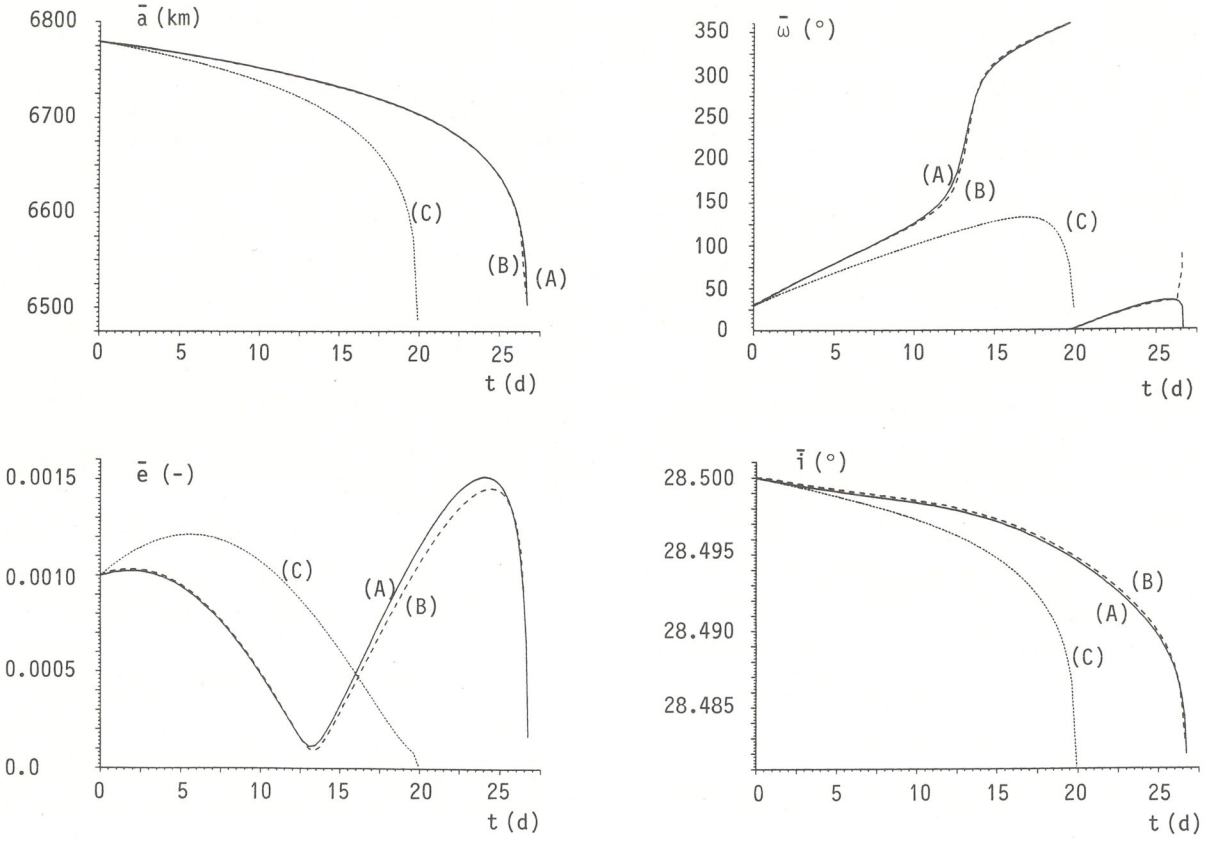

Fig.4-2 to 4-5: EURECA, time history of the mean semimajor axis $\bar{a}(t)$ (Fig.4-2), mean orbit eccentricity $\bar{e}(t)$ (Fig.4-3), mean argument of perigee $\bar{\omega}(t)$ (Fig.4-4), and mean orbital inclination $\bar{i}(t)$ (Fig.4-5) for predictions due to ...
(A) a numerical integration method, (B) the new analytical theory, and
(C) a simplified analytical theory assuming no short-periodic drag force variation (see Fig.4-1 for the relevant drag force model assumptions)

A good indicator for the accuracy by which out-of-plane airdrag perturbations due to the rotating earth atmosphere are modelled is the time history of the orbit inclination predictions. Fig.4-5 shows that also in this case the numerical (A) and the new analytical results (B) are in very good agreement, in contrast with results from a simple analytical theory (C).

Finally, the accuracy by which the short-periodic drag force variation is modelled (Fig.4-1), and by which the highly sensitive interaction between airdrag and geopotential perturbations is taken into account, is well monitored by the predictions of the mean eccentricity (Fig.4-3) and mean argument of perigee (Fig.4-4). The good agreement between the respective numerical predictions (A) and new analytical results (B) according to Fig.4-3 and 4-4 also verifies the separation-of-perturbations approach used in (3.10) for the determination of the effective mean time rates of change of the orbital elements. Especially noteworthy is the coherence of the predictions (A) and (B) in the vicinity of a reverse of the eccentricity development from a steep decrease to a steep increase of almost equivalent slope around day 13 of the simulation in Fig.4-3. The corresponding rapid shift of the mean perigee due to the impact of the small eccentricity on the airdrag and geopotential perturbation equations (especially due to odd zonal harmonics) can be noted in Fig.4-4. Within 2 days the mean perigee $\bar{\omega}$ drifts away from its initial position close to the diurnal density bulge, and its motion stabilises to the normal J_2 secular rate only after a 180° arc is covered, and the positions of perigee and apogee are exchanged with respect to the diurnal density distribution.

4.2 Orbit Prediction Accuracy in a Weakly Defined Perturbation Environment

The preceeding analysis demonstrated that the new analytical orbit prediction tool performs very accurately, if a perfect knowledge of the relevant orbit perturbation environment, especially as regards airdrag, can be assumed. In an operational environment, however, when analysing the decay of a close-earth satellite of unknown geometry and mass, and when attempting to predict its reentry into a future of unknown or uncertain solar and geomagnetic activity, the emphasis as far as modelling effort is concerned now lies on the derivation and extrapolation of the unknown airdrag parameters from available observation data. The most widely used data sources in this context are:

(1) NASA Prediction Bulletin Data, providing the satellite number and identification, and a set of mean Brouwer orbital elements

(2) Solar activity measurements and forecasts in terms of actual and mean 10.7cm solar fluxes, plus geomagnetic activity measurements and forecasts in terms Bartels A_p indeces

A feasable approach for the prediction of solar and geomagnetic activities into future (in lack of better models), is the use of a constant value of A_p = 4 (= most likely value), a solar flux model such as $F_{10.7} = F_{10.7}(t_o) = \text{const}$ or $F_{10.7} = F_{10.7}(t_o) + dF/dt \cdot (t-t_o)$ for short or medium term predictions (over less than one month), or a solar flux model such as $F_{10.7} = F_{10.7}(t_o) + \Delta F \sin(\nu \cdot (t-t_o))$ for long-term predictions, with pronounced solar cycle effects on $F_{10.7}(t)$.

In order to determine the satellite related airdrag parameters of an object of unknown geometry, mass, and attitude, one has to deduce the necessary information from a previously observed time history of the semimajor axis of the orbit. This can be accomplished by performing a least-squares fit to a set of data pairs $\bar{a}_k(t_k)$ to obtain a low degree polynomial approximation $\bar{a}(t)$.

$$\bar{a}(t) = a_0(t_o) + a_1(t-t_o) + a_2(t-t_o)^2 + a_3(t-t_o)^3 \qquad (4.1)$$

The corresponding decay rate at time t is

$$\dot{\bar{a}}(t) = a_1 + 2\,a_2\,(t-t_o) + 3\,a_3\,(t-t_o)^2 \qquad (4.2)$$

As $\dot{\bar{a}}$ is known to be only affected by airdrag, and as this rate is furthermore directly proportional to the ballistic parameter $B = c_D\,A/m$ (which contains all satellite related drag data), one can in a single step calibrate the airdrag perturbation equations via $\dot{\bar{a}}$ as to obtain the observed decay rate according to (4.2). - Another way to determine B is an iterative propagation of the orbit over an arc of known solar and geomagnetic activity between two sets of NASA 2-line elements, until B has been improved so far as to meet the observed value of the semimajor axis of the second data set with sufficient accuracy. This second approach is less liable to inaccuracies in the transmitted 2-line element sets, if the iteration is performed over a sufficiently long arc of 1 or 2 days. In lack of better information, the thus acquired value of B should be taken as constant until the next update.

The outlined orbit decay prediction method was for the first time employed within a quasi-operational environment at the occasion of the uncontrolled reentry of objects A and C of the Russian ocean surveillance satellite COSMOS 1402, after a failed separation and injection into a higher 1000km orbit of the nuclear reactor module of the spacecraft on Dec.28, 1982. The major fragments A and C of COSMOS 1402 (part B decayed within 2 days) were thereafter continuously tracked by NORAD, and the determined mean Brouwer orbital elements were regularly submitted in NASA 2-line format to several computation centres via NASA Prediction Bulletins. The diverging orbits of parts A and C, with 1402-A decaying at a much higher rate than 1402-C, suggested soon after reception of the first sets of elements that the heavy nuclear reactor was contained in part C. This assumption was in fact later confirmed by the launch authorities.

Starting from Jan.10 and Jan.14 respectively, Fig. 4-6 and 4-7 show results of a reentry prognosis for COSMOS 1402-A and 1402-C in terms of prediction error with respect to the actual reentry epochs as function of the date at which the prediction was performed. The results for COSMOS 1402-A illustrated in Fig.4-6 demonstrate that the prediction uncertainty almost linearly decreases while approaching the true reentry date, and that the uncertainty margins are of the order of 10% of the remaining lifetime of the spacecraft. This figure of 10%, reflecting both the uncertainties in the satellites area-per-mass ratio (which was in the range of 320 to 370kg/m² for COSMOS 1402-A), and in the predicted solar and geomagnetic activities, appears to be a widely accepted error estimate for medium and short-term reentry predictions.

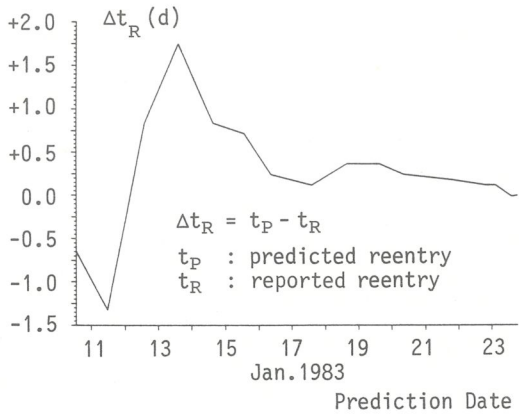

Fig.4-6: COSMOS 1402-A reentry prediction error as function of the prediction date. (reported reentry at t_R = Jan.23,22:21 UT)

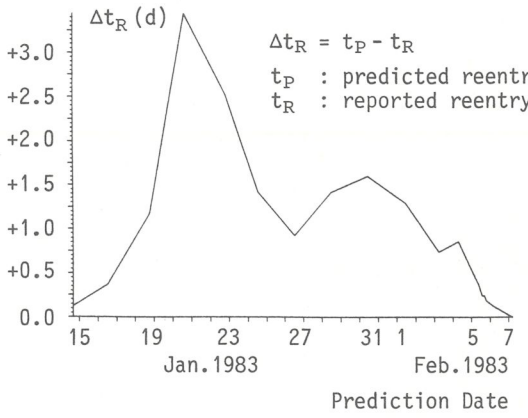

Fig.4-7: COSMOS 1402-C reentry prediction error as function of the prediction date. (reported reentry at t_R = Feb.7,11:10 UT)

Fig.4-7 shows a much larger fluctuation of the prediction error for the COSMOS 1402-C reentry as compared with COSMOS 1402-A. The corresponding range of estimated area-per-mass ratios extends from 600 up to 800kg/m². By inspection of Fig.4-7 one finds that the predicted reentry date until Feb.5 seems to settle at an epoch which is about 1 day beyond the actual splash-down. This phenpmenon finds its explanation in an outburst of geomagnetic activity on the afternoon of Feb.5 (A_p went up to 46), which reduced the expected lifetime by 1 day from 3 to 2 days.

In order to complete the picture, Fig.4-8 and 4-9 respectively show the aposteriori numerically computed splash-down locations for COSMOS 1402-A and 1402-C, using ballistic parameter estimates from previous analytical predictions, and using the last available NASA 2-line element information (which was only received after the actual reentries).

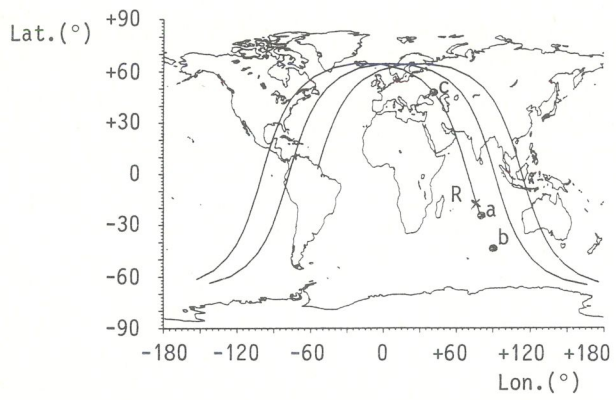

Last 2-line elem.	pred. splash-down
23.1.83 18:37 UT	23.1.83 22:22 UT ⇒ a
23.1.83 15:43 UT	23.1.83 22:26 UT ⇒ b
23.1.83 14:15 UT	23.1.83 22:02 UT ⇒ c
reported reentry	23.1.83 22:21 UT ⇒ R

COSMOS 1402-A

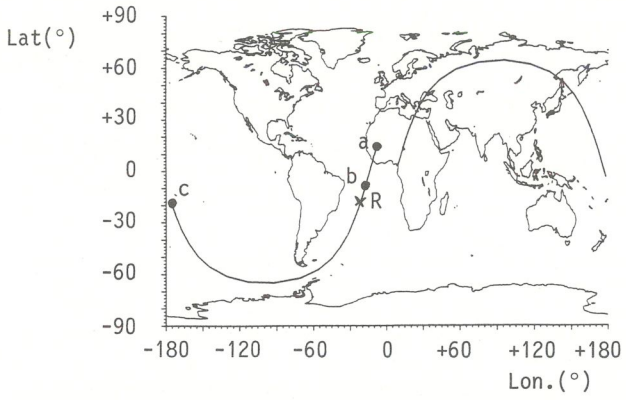

Last 2-line elem.	pred. splash-down
7.2.83 9:46 UT	7.2.83 11:18 UT ⇒ a
7.2.83 8:19 UT	7.2.83 11:11 UT ⇒ b
7.2.83 5:25 UT	7.2.83 10:35 UT ⇒ c
reported reentry	7.2.83 11:10 UT ⇒ R

COSMOS 1402-C

Fig.4-8 and 4-9: Reported splash-down versus numerically computed splash-down locations for COSMOS 1402-A (Fig.4-8, left) and COSMOS 1402-C (Fig.4-9, right) on the basis of the last three sets of published NASA 2-line elements.

4.3 Computing Time Requirements of the New Analytical Theory

The computing (CPU) time which is necessary to perform the prediction as depicted in Fig.4-2 to 4-5 by means of the new analytical orbit generator as implemented in the APODES program is of the order of 0.36s of CPU-time per orbit (= t_{ref}) on a CII/HB Series 66 computer for an initial step size of one revolution. Over a single orbit prediction interval this compares with about $t_{ref}/4.85$ for a simple analytical theory, and with about $t_{ref} \cdot 8.82$ for a fast numerical multi-step propagator.

Using a step-size control dependent on the actual decay rate $\dot{a}$, the CPU-time consumption of the new analytical technique can further be reduced to values of $t_{ref}/5.0$ up to $t_{ref}/15.0$, depending on the present orbit altitude and drag force level. For the decay prediction of EURECA (Fig.4-2), a step-size increase corresponding to an average CPU-time reduction down to $t_{ref}/7.0$ per orbit, results in an error for the predicted lifetime of only 2.7% .

As was initially claimed in Fig.1-1, the present analytical orbit theory is thus capable of predicting a close-earth satellite orbit of low to moderate eccentricity with an accuracy close to a numerical integration, and within a computing time close to that of a simple analytical method.

5. CONCLUSIONS

The present paper deployed the basic features of a new analytical orbit prediction method for close-earth satellite orbits under the influence of geopotential (J_2,J_3,J_4) and airdrag perturbations. Major concern was given to the accurate and yet integrable representation of the airdrag perturbation equations, taking into account a rotating earth atmosphere, a variable aerodynamic satellite cross-section, and an air density model as function of the atmospheric parameters altitude, latitude, local solar time, season, geomagnetic activity, as well as actual and mean 10.7-cm solar flux activity indices.

The new theory is especially suited for orbits of low to moderate eccentricities with altitudes between 120 and 1000km. The major applications are in the field of altitude decay predictions for mission analysis purposes, and in the field of splash-down forecasts for uncontrolled satellite reentries. When operated with a controlled step-size, the present method is capable of meeting the accuracy obtained by a fast numerical integrator within the computing time which is necessary for a conventional, simplified analytical orbit generator.

REFERENCES

1. H.H. Klinkrad
Analytical Computation of Close-Earth Satellite Orbits with a Realistic Drag Force Model
(in German)
Ph.D. Dissertation, Braunschweig University of Technology, Braunschweig/FRG, Nov.1983

2. H.H. Klinkrad, G. Janin
Orbit Prediction and Shuttle Rendezvous Strategy for EURECA
Acta Astronautica, Vol.10, No.10, pp.673-685, 1983

3. A.E. Hedin, et al.
A Global Thermospheric Model Based on Mass Spectrometer and Incoherent Scatter Data.
MSIS 1 - N_2 Density and Temperature
Journal of Geophysical Research, Vol.82, No.16, pp.2139-2147
MSIS 2 - Composition
Journal of Geophysical Research, Vol.82, No.16, pp.2148-2156

4. J.J.F. Liu, R.L. Alford
A Semi-Analytic Theory for the Motion of a Close-Earth Artificial Satellite with Drag
AIAA Paper No.79-0123, 17th Aerospace Sciences Meeting, New Orleans/La., Jan.15-17, 1979